Meso-Cenozoic Tectonothermal History of Permian Strata, Southwestern Weibei Uplift: Insights from Thermochronology and Geothermometry

YU Qiang[1, 2], REN Zhanli[3, 4, *], LI Rongxi[1, 2], TAO Ni[1, 4], QI Kai[3, 4], JIANG Cheng[5, 6] and WANG Baojiang[7]

[1] *The School of Earth Science and Resources, Chang'an University, Xi'an 710054, China*
[2] *Key Laboratory of Western China's Mineral Resources and Geological Engineering, Ministry of Education, Chang'an University, Xi'an 710054, China*
[3] *State Key Laboratory of Continental Dynamics, Northwest University, Xi'an 710069, China*
[4] *Department of Geology, Northwest University, Xi'an, 710069, China*
[5] *State Key Laboratory of Coal Mine Disaster Dynamics and Control, Chongqing University, Chongqing 400030, China*
[6] *State and Local Joint Engineering Laboratory of Methane Drainage in Complex Coal Gas Seam, Chongqing University, Chongqing 400030, China*
[7] *Research Institute of Yanchang Petroleum (Group) Company Limited, Xi'an, Sichuan, 710075, China*

Abstract: This study provides an integrated interpretation for the Mesozoic - Cenozoic tectonothermal evolutionary history of the Permian strata in the Qishan area of the southwestern Weibei Uplift, Ordos Basin. Apatite fission-track and apatite/ zircon (U-Th)/He thermochronometry, bitumen reflectance, thermal conductivity of rocks, paleotemperature recovery, and basin modeling were used to restore the Meso-Cenozoic tectonothermal history of the Permian Strata. The Triassic AFT data have a pooled age of ~180±7 Ma with one age peak and P(χ^2)=86%. The average value of corrected apatite (U-Th)/He age of two Permian sandstones is ~168±4 Ma and a zircon (U-Th)/He age from the Cambrian strata is ~231±14 Ma. Bitumen reflectance and maximum paleotemperature of two Ordovician mudstones are 1.81%, 1.57% and ~210°C, ~196°C respectively. After undergoing a rapid subsidence and increasing temperature in Triassic influenced by intrusive rocks in some areas, the Permian strata experienced four cooling-uplift stages after the time when the maximum paleotemperature reached in late Jurassic: (1) A cooling stage (~163 Ma to ~140 Ma) with temperatures ranging from ~132°C to ~53°C and a cooling rate of ~3°C/Ma, an erosion thickness of ~1900 m and an uplift rate of ~82 m/Ma; (2) A cooling stage (~140 Ma to ~52 Ma) with temperatures ranging from ~53°C to ~47°C and a cooling rate less than ~0.1°C /Ma, an erosion thickness of ~300 m and an uplift rate of ~3 m/Ma; (3) (~52 Ma to ~8 Ma) with ~47°C to ~43°C and ~0.1°C /Ma, an erosion thickness of ~500 m and an uplift rate of ~11 m/Ma; (3) (~8 Ma to present) with ~43°C to ~20°C and ~3°C/Ma, an erosion thickness of ~650 m and an uplift rate of ~81 m/Ma. The tectonothermal evolutionary history of the Qishan area in Triassic was influenced by the interaction of the Qinling Orogeny and the Weibei Uplift, and the south Qishan area had the earliest uplift -cooling time compared to other parts within the Weibei Uplift. The early Eocene at ~52 Ma and the late Miocene at ~8 Ma, as two significant turning points after which both the rate of uplift and the rate of temperature changed rapidly, were two key time for the uplift-cooling history of the Permian strata in the Qishan area of the southwestern Weibei Uplift, Ordos Basin.

Key words: low temperature thermochronology, fission track, (U-Th)/He, basin modeling, cooling history, uplift, Ordos Basin

Citation: Yu et al., 2019. Meso-Cenozoic Tectonothermal History of Permian Strata, Southwestern Weibei Uplift: Insights from Thermochronology and Geothermometry. Acta Geologica Sinica (English Edition), 93(6): 1647–1661. DOI: 10.1111/1755-6724.14367

1 Introduction

Paleogeothermal features and its evolution history have a strong relationship with regional geological tectonic features and geological movements (Allen and Allen, 2005). Great differences of thermal regime and tectonothermal history among several sedimentary basins in northern China have been reported (Ren et al., 1994). The Qishan area, located in the southwestern part of the Weibei Uplift, Ordos Basin (Fig. 1), has been under control of tectonothermal regime of the Qinling Orogen, the Ordos Basin and the Weihe Basin (Liu et al., 2005; Ren et al., 2014; Qi et al., 2015). It is a key area for research of the Meso-Cenozoic tectonothermal evolutionary history of the southwestern Ordos Basin (Ren et al., 2014). With the increasing petroleum exploration and exploitation in the Ordos Basin, more scientists are paying attention to the tectonic evolution and petroleum resource assessment in this region (Liu et al., 2005; Ren et

* Corresponding author. E-mail: renzhanl@nwu.edu.cn

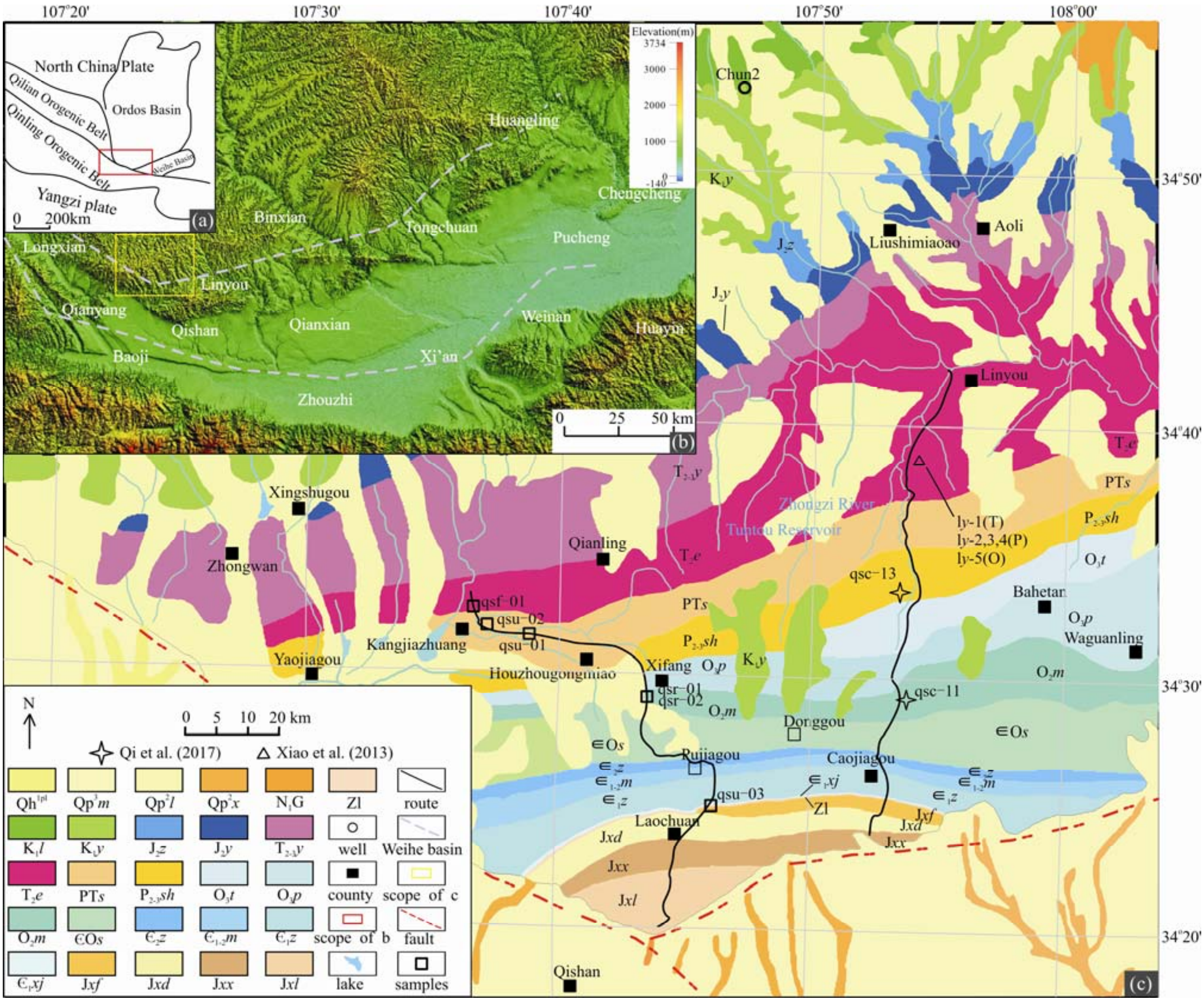

Fig. 1. (a) Locality map and (b) southwestern part of the Ordos Basin and Weihe Basin, with rectangle showing the study area. (c) Geological map and samples.

al., 2006; Ren et al., 2014).

The geothermal history has an important control on the generation, entrapment and accumulation of petroleum resources (Suggate, 1998). Tectonothermal evolution of several tectonic units inside and around the Ordos Basin had been discussed in previous studies with a greater understanding of the Yishan Slope but a relative poorer understanding of the Weibei Uplift. The paleo-geothermal history of the Yishan Slope, which records a relatively low thermal gradient from the Paleozoic to the Early Mesozoic, but an increasing geothermal gradient of 3.3–4.1°C/100 m and the terrestrial heat flow of 81– 95 mW/m^2 by the Late Mesozoic, followed by a rapidly decreasing heat flow to the present values which average 2.80°C/100 m and 63 mW/m^2 (Ren et al., 1994). Apatite fission-track thermochronology has been used by several researchers to determine the uplift and cooling history of the Weibei Uplift (Ren et al., 1994; Liu et al., 2005; Wang et al., 2010; Xiao et al., 2013; Qi et al., 2015; Huang, Ren, and Gao, 2016; Yu et al., 2018) with the a widely accepted opinion that the Weibei Uplift, which started as a part of the Ordos Basin before the Early Cretaceous, became a tectonic zone during the middle-late period of the Yanshanian Movement, and finally evolved as the present-day structure after the Himalayan Movement.

The Qishan area located at the southwest of the Weibei Uplift, north of the Weihe Basin and not far away from the Qinling Orogeny, may have a different evolution history compare to its north surrounding areas within the Weibei Uplift. There have been still many arguments about analysis of paleo-geothermal records and interpretation of cooling-denudation history of the Southwestern Weibei Uplift since the Mesozoic. All of these problems have restricted our understanding of the regional tectonothermal evolution history and the hydrocarbon exploration of the Weibei Uplift, which are further explored in this work.

2 Geological Background

The Ordos Basin, which lies to the east of the Helan-Longmenshan north-south tectonic belt, developed as a part of the North China Craton. The Ordos Basin had experienced several evolutionary stages including a basement stage (the Archean - the Proterozoic), a passive continental margin stage (the Early Paleozoic), a regional tectonic uplifting stage (the Caledonian - Hercynian), and a depression stage of the North China Craton (the Late Paleozoic) (Ren et al., 1994; Liu et al., 2006; Zhao et al., 2010; Gong et al., 2014).

It is generally accepted that the coal-bearing rocks in the Shanxi Formation (lower Permian) and the dark shale rocks in the Yanchang Formation (upper Triassic) are two important source rocks for the petroleum resources of the Ordos Basin (Yu et al., 2017). The Yanchang Formation forms a 1,000 − 1,300 m thick succession of detrital river-delta-lake sediments (Zhang et al., 2010; Yang et al., 2014; Fan et al., 2018; Shi et al., 2019) in a humid paleoclimate (Qiu et al., 2015a, 2015b). The Mesozoic hydrocarbon reservoirs in the Zhenjing area (southwestern Ordos Basin) were sourced mainly from black shales of the Yanchang Formation (Li et al., 2017; Qiu et al., 2013; Shi et al., 2019; Wang et al., 2017), which is also a resource for unconventional oil and gas (Yang et al., 2017).

The Qishan area is located in the southwest edge of the Weibei Uplift. It has a stabilized crystalline basement overlain by Middle and Upper Proterozoic, Cambrian, Ordovician, Carboniferous, Permian, Triassic, Jurassic, and Lower Cretaceous strata. The Upper Ordovician to Lower Permian periods and the Upper Cretaceous are missing on unconformities.

The lithology of the Qishan area are as follows: The strata of the Middle Proterozoic includes a set of gray-dark gray medium-thick dolomite and dolomitic limestone with chert nodules and a small amount of clastic rock. The Cambrian is a combination of predominantly thick oolitic limestone and microbid limestone mixed with calcareous shale, with minor of sandstone and shale deposits at the base. Ordovician includes the Majiagou Fomation, composed of mainly gray thick limestone mixed with dolomite and brecciated dolomite, with minor yellow-green, dark-gray shale and siltstone. The Middle Permian Shihezi Formation unconformably overlies the Middle Ordovician Majiagou Formation.

The Permian includes the Shihezi Formation and the Shiqianfeng Formation from the bottom to the top. The upper part of the Shihezi Formation consists of gray green, yellow-green pebbly sandstone, sandstone, siltstone, silty mudstone and siltstone, while the lower part consists of purple mudstone, silty mudstone and yellow-green sandstone. The Shiqianfeng Formation is predominantly composed of purple-red sandstone with pebbly, red-gray to green sandy mudstone. The Triassic includes the Ermaying and Yanchang Formations. The Ermaying Formation is composed of gray-green feldspathic sandstone and red mudstone. The Yanchang Formation consists of gray, gray-green sandstone and shale. The Jurassic and the Cretaceous are dominated by continental deposits, while the Quaternary deposits are loess.

3 Sample Collections

In this study, the Erlanggou section, which is located in Xifang village of the Qishan area and crosses several tectonic zones, was selected based on the 1:25 000 geological maps for field investigation and collection of fresh samples (Fig. 1). The section was chosen because it has fully exposed Middle Paleozoic to Cretaceous strata, and has been previously studied extensively for sedimentology, tectonics, geochemistry and geophysics (Chen et al., 2015; Qi et al., 2015; Ren et al., 2015a).

One sample of the qsf-01 was collected from the T_2e Formation to the north of the Kangjiazhuang county for apatite fission-track analysis. Two rocks of sandstone (qsu-01 and qsu-02) were collected from the exposed Permian strata in the area of Houzhougongmiao for apatite (U-Th-Sm)/He analysis and one sandstone (qsu-03) from the Cambrian for zircon (U-Th)/He analysis. Two mudstones (qsr-01 and qsr-02) were collected from the Ordovician in the Xifang area for the test of bitumen reflectance (Fig. 1). In each set of strata exposed in the field, samples of diverse lithology were collected for testing their thermal conductivity (Fig. 2). Sandstone samples for apatite fission-track and (U-Th)/He analysis weighed about 3−5 kg and were of moderate particle size.

4 Methods

Every method or technique has its limitations in data processing and geological interpretation. For example, accuracy and reliability of the apatite annealing technique for estimating buried temperatures varies depends in part on apatite chemical composition, which would result as different fission-track age calculation and interpretation (Gleadow et al., 2002). Even for the same sample by the same method, data and interpretation may vary between different laboratories. Vitrinite or bitumen reflectance data can only calculate the maximum paleotemperature, but cannot recover the cooling history. The apatite (U-Th-Sm) /He method needs improvement to alleviate the problem of excess He and He diffusivity issues. In view of the above, a multi-disciplinary integration of multiple methods has increasingly become an accepted approach for researching tectonothermal evolution (Ren et al., 1994; Yu et al., 2017; Tao et al., 2017).

Geothermometry measurements have been used including apatite fission-track, apatite (U-Th)/He, zircon (U-Th)/He, bitumen reflectance and rock thermal conductivity in this research with the procedure as follows: First, thickness of rocks removed by erosion was estimated using the thickness of strata in nearby stratigraphy sections, assuming there was no great difference in original depositional thickness. Second, the geological time of formation and the compaction correction model were used by previous work. Third, a geological model was established based on the theory of sedimentary basin recovery by modeling using the software *P*etromod. The compaction correction, the paleo-thickness and the burial subsidence calculation were

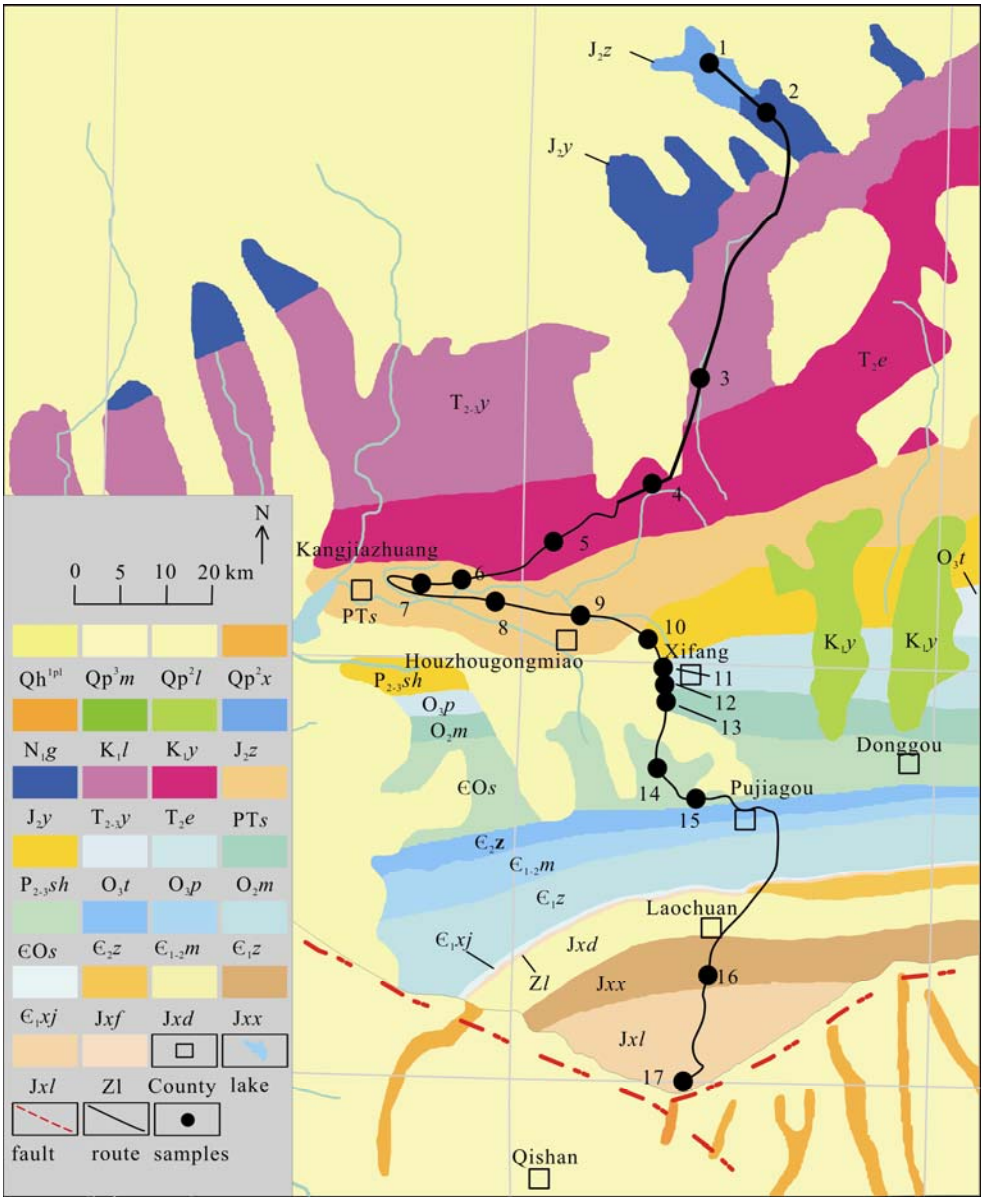

Fig. 2. Samples collected for determination of thermal conductivity (color of strata refers to Fig.1).

completed next. The maximum paleo-geothermal gradient was calculated using the geothermometry data including bitumen reflectance - maximum paleotemperature values, apatite fission track data and apatite/zircon (U-Th) /He data. All the methods mentioned above were used together to recover the rate and thickness of uplift and erosion, cooling rate of the Qishan area in the Mesozoic–Cenozoic using the HeFTy software (Ketcham, 2005). Basin modeling restricted by correction of stress and of *R*o for the Qishan area was made. Finally, comparison of tectonothermal history between the Qishan area and its surrounding regions was discussed.

4.1 Apatite fission-track analysis

Apatite and zircons grains for thermochronological analysis were separated from sandstones at the Shangyi Mineral-Rocks Technology Service Co., Ltd., Langfang, Hebei Province, China. Sample processing was conducted as follows: (1) samples were crushed to remove the dirt on the surface, diagenetic fractures such as inclusions and veins were avoided. (2) rock samples were crushed to 40 - 100 mesh depending on the lithology and texture of the rocks. (3) samples were separated using magnetic and heavy liquid separation techniques. A strong magnetic separation was used to remove the strongly magnetic particles. The weakly magnetic fraction was subject to electromagnetic separation to remove electro-magnetic minerals and to retain the non-magnetic minerals. (4) the non-magnetic minerals were separated by heavy-liquid separation and the heavy minerals were retained. (5) the heavy minerals were separated using high frequency dielectric and metal sulfides were removed and apatite were obtained. Finally, clean apatite and zircons were obtained by picking out impurities under a binocular microscope. Details for separation of zircon grains followed related research work reported by a number of researchers (Wang et al., 2016; Du et al., 2018; Song et al., 2018; Wang et al., 2018).

Unlike conventional the EDM method (Donelick et al., 2005; Ni et al., 2016; Pang et al., 2019), in which neutron irradiations are required, ^{238}U can be directly determined using the LA-ICP-MS method (Yang et al., 2017; Malusà and Fitzgerald, 2018; Kohn, Chung, and Gleadow, 2019). Apatite fission-track analysis was carried out at the Thermochronology Laboratory of the University of Melbourne. More than 1000 apatite grains separated from the sample qsf-01 were mounted in epoxy resin on a glass slide of 3 cm ´ 2.5 cm. The slice was ground to make sure most of the grains were exposed at or near the surface using a Struers 1200# piano plate and polished on a rotating lap with different grades of diamond paste (e.g. 6, 3 and 1 μm). Spontaneous tracks of apatite grains in polished mounts were revealed by etching in 5M HNO_3 at 20°C for 20 s.

After coating with a thickness of 5 nm gold for the slide in a vacuum unit, the grains parallel to prismatic crystal faces were selected and fission tracks were selected under the microscope (Zeiss Axio Imager M1m) at a magnification of ×1000. High-resolution images of pixel-size (~0.0698–0.0705 μm /pixel) for each grain recorded under both transmitted and reflected light were saved and stacked relatively for track counting and density analysis. Using only etch pits from spontaneous tracks, the measured Dpars for each grain from which age or length data were collected.

Using an UP-213 laser and an Agilent 7700 LA-ICP MS (Laser Ablation Inductively Coupled Plasma Mass Spectrometer) with 5 Hz repetition rate, ~2.0 J/cm^2 energy, 30 μm diameter beam size and lasting for 25 s, the ablation and uranium analysis of each selected grains was carried out together with NIST 612, Mud Tank and Durango apatite for calibration.

The software RadialPlotter with the version of 9.4 (Vermeesch, 2009) was used to analyze the distribution of AFT grain ages, their peaks and radial features.

4.2 (U-Th)/He analysis

Unlike fission tracks method, in the lower temperature (U-Th) /He dating system, the isotope ^4He produced by alpha decay would gradually dissipate out of the crystals at higher temperatures. In other words, it can be significantly preserved within crystals only at lower temperatures, typically ranging 40°C–85°C for apatite (Farley, 2000) and 170°C–190°C for zircon (Reiners, Farley and Hickes, 2002). With the recorded closed temperature, the (U-Th) /He age can be used to interpret the history of tectonothermal evolution as the “Thermal Clock” of apatite/zircon would start when the temperature of samples decreases to the closure temperature. The time-temperature evolution, erosion rate and cooling rate of geological units can be calculated by the geological time of the “Thermal Clock”, the closure temperature and the paleogeothermal gradient (Hu et al., 2008; Qiu et al., 2010; Ren et al., 2015b; Chen et al., 2018).

Apatite separates selected were sent to the Isotope Thermochronology Laboratory of the Chinese Academy of Geological Sciences for measurement. Sample processing was conducted as follows: (1) Each apatite crystal with good crystal shape, no fissures or inclusions were selected using a binocular microscope. (2) Photo-micrographs were taken and crystal size was measured, calculating the α - correction coefficient of the particles. (3) The crystals were put into platinum capsules. The helium gas was heated and collected in the Diode Laser (970 nm) with the temperature of 900^{o}C and analyzed in the Helium Isotope Ratio Mass Spectrometer (Alphachron II). The content of ^4He was measured in the diode lasers with the accuracy less than 1% and the ratio of $^4He/^3He$ was measured by means of Quadrupole Mass Spectrometer. (4) After that, the apatite samples were added to diluent which has a concentration of 15 ppb ^{235}U and concentration of 5 ppb ^{230}Th. (5) Meanwhile, the equal amount of diluent should be added to the standard solution which has 25 ppb ^{235}U and 25 ppb ^{230}Th. The apatite will be dissolved by the nitric acid as 7 mol/L in the diluent solution. (6) After the apatite fully dissolved and water added, the U and Th content could be obtained by the ICP-MS. The accuracy of isotope ratio of U and Th is limited within 2%, and check samples of Durango apatite reference material (McDowell et al., 2005) was also run with the samples.

Selected zircon separates were sent to the Thermochronology Laboratory of the University of Melbourne. Euhedral and clear zircon grains with no inclusions were selected under polarized light from grains previously immersed in ethanol. Protocols for laser He extraction/analysis (House et al., 2002) were taken. After being loaded into platinum tubes of an optically coupled diode laser with a wavelength of 820 nm, zircon separates were outgassed in the vacuum with the temperature of 1300°C for 15 minutes. ^4He abundances could be calibrated and calculated by ^3He spike dilution with an uncertainty less than 1%. Grains were digested in HF spiked with ^{233}U and ^{229}Th for 40 hours at the temperature of 240°C and a same amount of spike with blank reagent was used as a standard solution. Using HCl for 24 hours at the temperature of 200°C, the second treatment of digestion for the grains was taken to dissolute the fluorides. After the dilution of solutions with the acidity of 10%, the U and Th content of zircon grains were analyzed on an ICP-MS (Agilent, 7700). The uncertainty of the (U-Th)/He experimental operation for this laboratory is estimated to be less than 6.2% (±1σ) (Li et al, 2015).

4.3 Bitumen reflectance analysis

Vitrinite reflectance value refers to the percentage between the reflected light intensity and the vertical incident light intensity of the polished surface of vitrinite with the wavelength of 546 nm. Currently, it is believed that with the increase of temperature, the maturity of source rocks increases (Zuo et al, 2017). Therefore, vitrinite reflectance can be used as an indicator to calibrate the degree of thermal maturity. As there is little vitrinite in the Ordovician carbonates, the bitumen reflectance would be the substitute indicator to evaluate the maturity of source rocks.

The bitumen reflectance of mudstone was measured at the Geochemistry Laboratory of Yangtze University. Before testing, the epoxy and sample were mixed and hardened, and then the sample was prepared as a polished thin section. Sections were polished and inspected under × 20 microscope in order to make sure there are stainless with few needle-like scratches, few pockmarks and clear boundaries among components for the testing. The reflectivity can be determined only after the qualified polished section enclosed in the dryer for 12 hours.

Bitumen reflectance measurements were made under dust and shock-proof conditions with steady illumination, and humidity less than 70%. After dipping the experimental liquid onto the surface of the polished section which has been parallelly fixed on the microscope stage, the testing points were selected from areas with no defects or mineral inclusions. During measurement areas of highly reflective material such as pyrite and inertinite were avoided. Selected points for measurement were distributed across the polished section. Due to slight differences of optical properties among particles in the

Table 1 Apatite fission-track length data, sample of qsf-01

ID	L_{app} (μm)	dz (μm)	L_{True} (μm)	Azimuth	Dip	Angle	Dpar (μm)	SD
Length01	14.49	3.44	14.89	44.41	13.34	45.97	1.99	0.2
Length02	11.76	2.94	12.12	80.93	14.06	81.2	2.15	0.22
Length03	10.15		10.15	57.51	0	57.51	2.11	0.08
Length04	14.72		14.72	77.99	0	77.99	2.43	
Length05	10.96	1.47	11.06	72.68	7.65	72.84	1.65	0.19
Length06	12.45		12.45	79.85		79.85	1.81	0.14
Length07	10.94	0.98	10.98	72.28	5.13	72.35	1.73	0.25
Length08	10.3	0.49	10.31	45	2.73	45.06	1.81	0.14
Length09	12.57	2.94	12.91	83.99	13.18	84.15	2.33	0.45
Length10	13.31	1.96	13.46	64.61	8.39	64.9	1.76	0.17
Length11	13.72	5.89	14.93	78.38	23.23	79.33	1.98	0.36
Length12	13.22	1.47	13.3	40.12	6.36	40.54	1.57	0.46
Length13	9.43	2.45	9.74	58.71	14.59	59.83	1.73	0.14
Length14	13.59	0.49	13.6	82	2.07	82.01	2.09	0.3
Length15	12.84	2.45	13.07	65.93	10.82	66.39	1.84	0.32
Length16	12.89		12.89	11.86		11.86	2.47	
Length17	13.01	0.98	13.05	41.2	4.31	41.39	1.8	0.1
Length18	11.7	1.47	11.79	52.28	7.17	52.62	1.34	0.27
Length20	11.7		11.7	74.77		74.77	1.55	0.1
Length21	7.85	0.49	7.86	85.32	3.58	85.33	1.71	0.1
Length23	12.05	0.98	12.09	64.39	4.66	64.49	1.56	0
Length24	10.55	1.47	10.65	72.76	7.95	72.93	1.69	0.2
Length25	13.33	0.49	13.34	5.26	2.11			
Length26	9.63		9.63	43.53	0			
Length27	7.75	2.45	8.13	35.84	17.56			
Length28	8.77	1.47	8.89	45.81	9.53			
Length29	11.11	2.45	11.38	46.27	12.45			
Length30	9.78	4.42	10.73	88.98	24.31	89.07	1.51	0.2
Length30	10.81	2.45	11.08	31.12	12.79	33.4	1.51	0.2
Length31	12.31	0.49	12.32	66.54	2.28	66.56	1.86	
Length32	14.28	5.89	15.45	63.47	22.41	65.61	2.88	0.33
Length33	14.34	1.96	14.48	86.51	7.79	86.54	2.01	0.1
Length33	15.7	0.49	15.71	28.56	1.79	28.61	2.01	0.1
Length35	13.47	4.91	14.34	71.1	20.02	72.28	4.68	5.52
Length36	12.23	0.49	12.24	80.13	2.3	80.14	1.8	0.1
Length37	12.79		12.79	85.3		85.3	1.86	0.2
Length38	10.71	1.47	10.81	52.29	7.83	52.7	1.6	0.4
Length40	11.44	0.49	11.45	75.62	2.46	75.63	2.1	0.45
Length41	13.97		13.97	45.47		45.47	1.98	
Length43	7.17	1.47	7.32	63.64	11.61	64.22	2.16	0.09
Length44	13.95	4.42	14.63	56.2	17.57	57.97	1.67	0.09
Length45	11.18	0.98	11.22	50.12	5.02	50.3	1.46	0.27
Length46	10.12	2.94	10.54	63.81	16.22	64.93	1.61	0.25
Length47	11.14		11.14	80.98		80.98	1.46	0.1
Length48	12.08	0.49	12.09	37.37	2.33			
Length49	13.7	2.45	13.92	52.21	10.16	52.9	1.61	0.18
Length50	10.87	0.49	10.88	68.26	2.59	68.28	2.05	0.09
Length51	10.58		10.58	52.37	0	52.37	1.8	0.27
Length52	13.2	0.49	13.21	25.89	2.13	25.97	1.69	0.53
Length53	10.48		10.48	87.5		87.5	1.51	0.1
Length54	12.15		12.15	64.58		64.58	1.49	0.1
Length55	12.11	1.96	12.27	45.39	9.21	46.11	1.66	0.1
Length56	11.87	0.49	11.88	34.32	2.37	34.39	1.53	0.28
Length57	11.59	4.91	12.59	37.04	22.94	42.69	1.48	0.17
Length58	13.45	1.96	13.59	63.25	8.31	63.55	1.47	0.2
Length59	13.13	1.47	13.21	67.9	6.4	68.04	2.44	0.5
Length61	12.72	3.93	13.31	76.07	17.15	76.7	1.84	0.32
Length62	11.64	4.91	12.63	52.97	22.87	56.3	2.01	0.16
Length63	13.82	3.93	14.37	62.14	15.86			
Length64	11.77	2.94	12.13	75.49	14.05	75.93	2.11	0.35
Length65	13.12	1.96	13.27	69.87	8.51	70.1	2.04	
Length67	10.7	3.44	11.24	51.54	17.8	53.69	2.06	0.31
Length68	11.87	0.98	11.91	84.56	4.73	84.58	2.42	0.24
Length69	9.32	0.49	9.33	53.26	3.02	53.32	2.06	0.09
Length70	11.78		11.78	81.28		81.28	1.62	0.28
Length71	12.57	5.4	13.68	68.43	23.24	70.25	1.19	0.35
Length73	12.37		12.37	53.13		53.13	1.82	0.24
Length74	12.88		12.88	74.01		74.01	1.61	
Length75	11.98	0.49	11.99	85.49	2.35	85.5		
Length76	12.11	0	12.11	67.86		67.86	1.64	0.14
Length78	13.35	0.49	13.36	67.14	2.1	67.16	1.54	0.2
Length79	13.6		13.6	53.98		53.98	1.7	0.1
Length80	12.76	2.45	12.99	63.92	10.89	64.42	1.76	0.19
Length81	11.87	0.98	11.91	73.05	4.73	73.11	1.4	0
Length82	12.22	1.96	12.38	48.76	9.12	49.39	1.63	0.11
Length83	12.88	0.49	12.89	51.82	2.18	51.85	1.66	0.14
Length86	12.26	0.98	12.3	79.81	4.58	79.85	2.11	0.16
Length88	14.84	1.47	14.91	79.98	5.67	80.03	2.15	0.27
Length89	14.75	2.45	14.95	73.5	9.45	73.73	2.1	0.17
Length90	14.27	0.49	14.28	34.94	1.97	34.99	2.04	
Length92	13.77	0.98	13.81	71.01	4.08	71.06	2.02	0.51
Length93	8.15	3.44	8.85	89.38	22.85	89.43	1.73	0.17
Length94	9.62	1.96	9.82	69.32	11.54	69.75	1.84	0.16
Length95	11.82	0.98	11.86	58.04	4.75	58.16	1.94	0.07
Length96	11.12		11.12	64.93		64.93	2.06	0.68
Length97	11.22	0.49	11.23	61.57	2.5	61.6	1.62	0.22
Length98	11.14	0.98	11.18	41.19	5.04			
Length99	11.53	1.96	11.7	88.26	9.66	88.29	1.92	0.3
Length100	12.49	0.98	12.53	24.93	4.49	25.3	1.83	0.1
Length101	14.3	1.96	14.44	17.77	7.82	19.36	1.69	0.2
Length102	13.45	1.96	13.59	58.56	8.31	58.93	1.57	0.3
Length103	12.82	1.47	12.91	83.75	6.55	83.79	1.57	0.35
Length104	12.95	3.44	13.4	55.07	14.86	56.4	1.53	0.28
Length105	12.5		12.5	65.03		65.03	1.53	0.51
Length107	12.68	0.49	12.69	55.29	2.22	55.32	1.52	0.2
Length108	8.21	5.89	10.1	72.07	35.66	75.51	1.58	0.3
Length110	11.78	0.98	11.82	86.07	4.76	86.08	1.55	0.1
Length111	15.09	0.98	15.12	37	3.72	37.16	1.46	0.1
Length112	11.14		11.14	33.24		33.24	1.31	0.37

Table ID: length name; Lapp(μm): apparent length; dz (μm): corrected z depth; LTrue(μm): true length; azimuth: azimuth dip; angle: angle to CAxis; DPar: average DPar(μm); SD: DPar Std Deviation.

same sample, more than 20 points were measured for each sample were made to ensure accuracy (Table 1).

Using the formulas Ro=0.3195+0.6790Ro_b (r=0.996, F=1024.888) from regression analysis of the relationship between bitumen reflection (Ro_b) and vitrinite reflection (Ro) (Feng and Chen, 1988), the tested bitumen reflection values were calculated to the vitrinite reflection.

4.4 Thermal conductivity analysis

Thermal conductivity data of samples was measured at the Geothermal Laboratory of the Department of Geology, Northwestern University. The TC 3000 thermal conductivity meter, which has the measuring range of 0.001–20 W/(m.K), resolution of 0.0005 W/(m.K) and accuracy of ±3% was used. The measurement parameters were diffusion coefficient of 0.00001 m^2/s, voltage of 1.5 V, and acquisition time of 5 s. According to the principle of the transient hot wire test and the requirements of GB/T 10297-2015 (test method for thermal conductivity of nonmetallic solids), two identical specimens were required for each geological sample measured (Yu et al., 2017). Each specimen weighed >1 kg, with a thickness > 0.3 mm, and a length > 2.5 cm.

5 Results

5.1 Apatite fission track data

The apatite fission-track sample (qsf-01) has 14 grains for measurement including number of spontaneous tracks (Table 1), area, density, content of ^{238}U, Dpar and calculated age for each grain (Table 2).

The AFT ages from 14 grains range from 132.12 Ma to 246.09 Ma with one age peak and the Dpar from 1.53 μm to 2.29 μm (Fig. 3). As the P(χ^2) >5%, the pooled age of ~180±7 Ma would be the cooling age of the sample qsf-01.

5.2 Apatite (U-Th)/He ages

A total of 9 apatite (U-Th) /He ages were obtained from two samples (Table 3). For sample of qsu-01, the corrected ages of four grains range from 146.04 Ma to 179.30 Ma except for the particles of qsu-01-02. The corrected ages of the three grains of qsu-01-03, qsu-01-04 and qsu-01-05 were relatively consistent. For the sample of qsu-02, the data obtained for the qsu-02-03 and qsu-02-04 grains are close, with an average age of 175.95 Ma. The above data demonstrate that the correct ages of the two samples of the Permian were relatively consistent, range between 167.00 Ma and 168.00 Ma. Thus, ~168±4 Ma was selected as the (U-Th)/He corrected age of Permian for the Qishan area.

The tested data of standard Durango samples (McDowell et al., 2005) indicated that the results are highly reliable and can be used in low-temperature thermochronology analysis and interpretation (Table 4).

5.3 Zircon (U-Th)/He ages

Using the Fish Canyon Tuff as a standard, the zircon (U-Th)/He age of Cambrian sample qsu-03 was determined. The corrected age can be divided to two groups (Table 5). The corrected ages of qsu-03-02, qsu-03-03, and qsu-03-04 are closely ranging from 231.1 Ma to 264.9 Ma, while the grain qsu-03-01 has the age of 183.1 Ma. Considering the 231.1 Ma and 246.5 Ma are closer than 264.9 Ma and

Table 2 Apatite fission-track age data, sample of qsf-01

No.	N_S	Area (cm^2)	ρS cm^{-2})	^{238}U(ppm)	±	1σ	Dpar(μm)	Age (Ma)	±	1σ
1	13	1.755E-05	7.409E+05	8.25	±	0.74	1.65 ± 0.48	184.18	±	53.69
2	19	1.134E-05	1.676E+06	14.50	±	1.10	1.53 ± 0.22	236.09	±	57.05
3	18	6.046E-06	2.977E+06	46.20	±	2.60	2.29 ± 0.51	132.68	±	32.15
4	27	1.773E-05	1.523E+06	15.60	±	1.10	1.69 ± 0.27	199.97	±	40.99
5	42	1.249E-05	3.362E+06	32.30	±	1.70	1.75	212.99	±	34.72
6	41	1.170E-05	3.504E+06	36.50	±	2.60	1.75	196.69	±	33.76
7	29	1.126E-05	2.576E+06	32.10	±	2.50	1.64 ± 0.10	164.83	±	33.19
8	31	7.646E-06	4.055E+06	63.20	±	4.40	1.98 ± 0.20	132.12	±	25.45
9	25	2.338E-05	1.069E+06	11.63	±	0.86	1.67 ± 0.25	188.44	±	40.18
10	72	1.288E-05	5.588E+06	60.10	±	3.40	1.87 ± 0.27	190.59	±	24.91
11	24	2.533E-06	9.475E+06	107.40	±	5.90	1.85 ± 0.37	180.97	±	38.26
12	20	4.043E-05	4.947E+05	5.97	±	0.67	2.13 ± 0.24	170.13	±	42.56
13	37	1.225E-05	3.022E+06	37.50	±	2.70	1.85 ± 0.10	165.51	±	29.70
14	20	1.420E-05	1.408E+06	14.80	±	1.10	2.08 ± 0.12	194.94	±	45.94
	418	2.014E-04	2.962E+06	34.72	±	27.91[a]	1.84 ± 0.22[a]			

[a] Standard deviation of mean.

Table 3 He age of apatite, samples of qsu-01 and qsu-02

Sample	^{4}He (ncc)	+/-	U (ppm)	+/-	Th (ppm)	+/-	Th/U	FT	Mass (μg)	U.Age (Ma)	F. Age (Ma)	+/-	S (μm)
qsu-01-01	0.19328	0.00485	7.78	0.22	93.84	2.49	12.37	0.53	0.69	77.21	146.04	2.53	29.9
qsu-01-02	0.56219	0.01407	18.70	0.52	25.11	0.67	1.38	0.65	1.31	142.42	219.91	4.73	37.3
qsu-01-03	1.09282	0.02734	41.09	1.15	85.72	2.24	2.14	0.65	1.34	108.70	167.55	3.51	38.0
qsu-01-04	0.27916	0.00700	7.84	0.22	64.19	1.69	8.40	0.59	1.01	98.71	167.74	3.16	33.9
qsu-01-05	0.58492	0.01464	31.16	0.86	43.48	1.15	1.43	0.62	1.04	111.14	179.30	3.67	34.6
qsu-02-01	5.29463	0.13335	176.94	4.90	225.11	5.86	1.31	1.00	3.03	62.51	62.51	2.07	49.2
qsu-02-02	2.20699	0.05629	12.12	0.34	41.15	1.07	3.48	0.80	8.78	94.49	117.92	3.02	68.3
qsu-02-03	3.54590	0.08871	26.83	0.75	82.27	2.14	3.15	0.76	4.51	139.07	183.54	4.41	55.8
qsu-02-04	8.09551	0.20243	119.50	3.32	111.22	2.90	0.95	0.74	3.65	124.75	168.36	4.23	50.3

Note: FT is the corrected factor, F. Age = Uncorrected Age (U.Age)/FT, F. age = alpha ejection correction age.

the qsu-03-02 has lower value of error 14.3, the age of ~230±14 Ma should be considered as the zircon He value for the Cambrian in the Qishan area.

5.4 Bitumen reflectance and thermal conductivity data

The calculated values of vitrinite reflectance of the two Ordovician mudstone samples are 1.55% and 1.39% (Table 6), which belongs to the stage of high maturation and hydrocarbon generation. This indicates that the Ordovician had experienced high paleotemperature in geological history. With the relationship between the maximum burial temperature (Tmax) and the average vitrinite reflectance (*R*o): Ln(*R*o)=0.0078Tmax–1.2 (Barker et al, 1986), the vitrinite reflectance data of samples (Table 6) were used to calculate the maximum paleo-temperature. The results show that two Ordovician mudstone samples experienced maximum paleo-temperature between ~210°C and ~196°C.

Thermal conductivity of various type of rocks shows that thermal conductivity of different lithologies varies greatly (Table 7). Dolomite in the Jixian System of the Proterozoic has the highest thermal conductivity, and values of sandstone are higher than that of mudstone. These data were input into the geological model of the Qishan area, which would objectively reflect the thermal conductivity of each set of sedimentary strata.

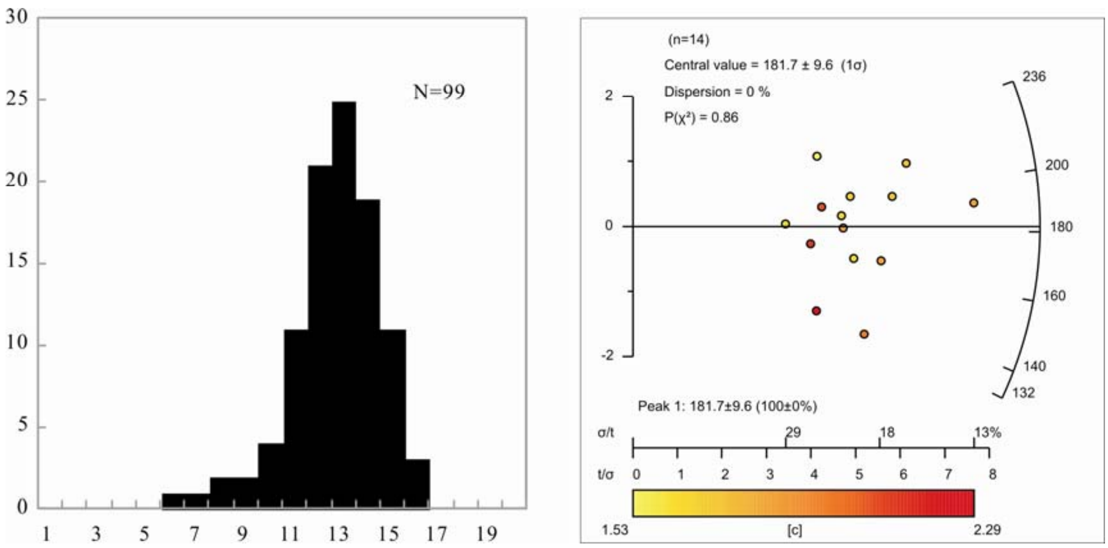

Fig. 3. AFT length and age distributions of qsf-01.
(a) AFT length; (b) AFT age ([c]=Dpar values).

Table 4 (U-Th)/He age of apatite Durango standard

Sample	^{4}He(ml)	+/-	U(ppb)	+/-	Th(ppb)	+/-	Th/U	Age(Ma)	+/-
DUR -34	0.2233	0.0056	0.0091	0.0003	0.1960	0.0051	22.0	33.2	1.1
DUR -48	0.2420	0.0061	0.0118	0.0003	0.2369	0.0062	20.6	29.4	1.0
DUR -55	0.2054	0.0052	0.0090	0.0003	0.1780	0.0046	20.2	33.1	1.1
DUR -56	0.2585	0.0065	0.0117	0.0003	0.2407	0.0063	21.0	31.0	1.0

Table 5 He age of zircon, sample of qsu-03

Sample	Lab. No.	He#	^{4}He (ncc)	Mass (mg)	^aF_T	U ppm	Th ppm	Th/U ratio	^{b}[eU] ppm	Corrected age (Ma)	Error (±1s)	Grain length (mm)	Grain half width (mm)	^{c}Crystal morphology
qsu-03-01	20232	67636	49.603	0.0021	0.70	973.7	312.5	0.32	1047.2	183.1	11.4	134.5	37.5	2T
qsu-03-02	20233	67639	9.141	0.0016	0.67	166.4	157.6	0.95	203.4	231.1	14.3	109.5	41.3	2T
qsu-03-03	20234	67642	21.620	0.0012	0.68	573.1	131.1	0.23	603.9	246.5	15.3	97.9	39.2	2T
qsu-03-04	20235	67645	46.363	0.0009	0.57	1567.6	350.6	0.22	1650.0	264.9	16.4	127.4	21.9	2T
Fish Canyon Tuff standard														
FCT	20460	67704	4.269	0.0035	0.73	311.1	202.9	0.65	358.7	28.0	1.7	177.5	39.5	2T
FCT	20461	67707	5.958	0.0043	0.76	361.4	182.9	0.51	404.4	28.1	1.7	197.5	40.9	2T

Fish Canyon Tuff Standard after Gleadow et al (2015)
[a]FT is the α-ejection correction after Farley et al. (1996).
[b]Effective uranium concentration (U ppm+0.235 Th ppm).
[c]Grain morphology - 0T = no terminations, 1T = one termination, 2T = 2 terminations.

Table 6 Results of bitumen reflectance of mudstone and maximum paleo-temperature

Sample number	Ro_b min(%)	Ro_b max(%)	Ro_b ran(%)	Standard eviation	Measurement points	Calculated *Ro* (%)	Calculated Tmax (°C)
qsr-01	1.55	2.19	1.81	0.1758	43	1.55	209.9
qsr-02	1.46	1.72	1.57	0.0985	6	1.39	195.7

Table 7 Thermal conductivity of different lithologies in the Qishan area

Sampling Location in figure 2	Sample numbers	Formation	Lithology	Thermal conductivity (W/m*K)	Specific heat capacity (kJ/kg*K)
1	qs-08-1	Jurassic	Grey fine sandstone	1.659	0.1929
2	qs-08-2		Silty mudstone	1.265	0.1467
3	qs-06-3	Triassic	Grey fine sandstone	3.793	0.1685
4	qs-06-4		Grey shaly sandstone	1.998	0.2283
5	qs-07-2		Dark gray shale	1.224	0.1705
6	qs-kjz01-2	Permian	Dark shaly sandstone	2.498	0.2289
7	qs-xf-04-8-1		Purple gray silty mudstone	0.053	0.1647
8	qs-xf-04-8-3		Purple gray fine sandstone	1.546	0.1616
9	qs-xf-04-8-4		Purple gray fine sandstone	1.798	0.1965
10	qs-xf-04-8-5		Purple gray fine sandstone	2.506	0.1929
11	qs-05-1	Ordovician	Gray argillaceous siltstone	2.563	0.2563
12	qs-05-2		Conglomerate	1.897	0.1898
13	qs-05-3		Grey shaly sandstone	1.726	0.1726
14	qs-03-1	Cambrian	Dark gray oolitic limestone	2.309	0.231
15	qs-03-2		Black shale	1.467	0.1467
16	qs-01-11-12	Proterozoic	Black massive powdery algal dolomite	3.637	0.3638
	qs-01-13-14		Dark gray mudstone	3.179	0.3179
	qs-01-1		Black massive powdery algal dolomite	3.529	0.353
	qs-01-2		Black massive powdery algal dolomite	4.967	0.4968
	qs-01-3		Black massive powdery algal dolomite	3.637	0.3255
	qs-01-4		Black massive powdery algal dolomite	3.052	0.3052
	qs-01-5		Black massive powdery algal dolomite	3.55	0.355
	qs-01-6		Black massive powdery algal dolomite	4.625	0.4625
	qs-01-7		Black massive powdery algal dolomite	4.766	0.4766
17	qs-02-1		Grey Dolomites	4.266	0.4267
	qs-02-2		Gray white algae layer dolomite	2.238	0.2239
	qs-02-3		Gray thick layered siliceous band dolomite	3.131	0.3131
	qs-02-4		Gray thick layered siliceous band dolomite	5.161	0.5161
	qs-02-5		Gray thick layered siliceous band dolomite	3.321	0.3321
	qs-02-6		Gray siliceous band dolomite	3.908	0.3908

6 Discussion

In the reconstruction of tectonothermal evolutionary history, the cooling history of samples and the uplift-denudation of strata will be discussed separately.

6.1 Cooling history reconstruction

Based on measured fission-track ages, track lengths and kinetic parameters (Ketcham, 2005), the HeFTy program was used to model the thermal history of sample sqf-01, qsc-13 and qsc-11 respectively (Fig. 5). Thermal history of the fission tracks was simulated using the annealing model (Laslett et al., 1987). Monte Carlo simulations were used to simulate 10000 temperature paths randomly.

Geological constraints are as follows. For the sample of qsf-01, continuous sedimentation from late Permian to late Triassic (~220 Ma) featured as source rocks and coal strata deposits relatively, constraint of 210–150 Ma (measured AFT ages ±30 Ma) and 60°C–120°C for the maximum temperature, and 10°C–80°C during 50 Ma – present for the rational uplift since early Eocene. Constraints for the sample of qsc-13 and qsc-11 have similar criterions. The data of the sample reflects the actual geological evolution process only if high degree of fitting was obtained. For the modeling results (Fig. 4), the white-grey zones had acceptable thermal history traces (50% > GOF > 5%). The gred zones had good thermal history traces (GOF ≥ 50%), and the best thermal history path for each sample was displayed in black inside the grey zones (Fig. 4).

Analysis shows that the modeled ages of the three samples were 182 Ma, 150 Ma, 124 Ma, and the GOF of 0.86, 0.52, 0.76, respectively. Meanwhile, the modeled lengths were 12.03±1.97 μm, 12.49±1.02 μm, 12.40±1.87 μm, and the GOF of 0.97, 0.54, 0.41, respectively. The results showed that modeling reliability of the qsf-01 and the qsc-13 were high enough to give highly acceptable paleotemperature evolutionary histories to the Triassic strata and the Permian strata of the Qishan area.

As the samples of qsc-11, qsc-13 and qsc-11 belong to different strata and geographically separated from each other, the comparison analysis should be discussed. (U-Th)/He age and the calculated Tmax values were added to the corresponding samples, and the best temperature paths for every sample were compared (Fig. 5). It can be seen that the Triassic, the Permian and the Ordovician strata where the three samples are located have roughly similar tectonothermal evolution, and all of them have gone through five stages of temperature evolution. Their differences mainly reflected in the cooling period, amplitude and rate.

Temperature evolution of the qsf-01 were: from its deposition to ~163 Ma increasing to ~114°C, fast cooling to ~79°C at ~148 Ma, slightly change to ~72°C at ~52 Ma, from ~52 Ma to ~6 Ma decreasing to ~58°C, ~6 Ma to present at ~20°C.

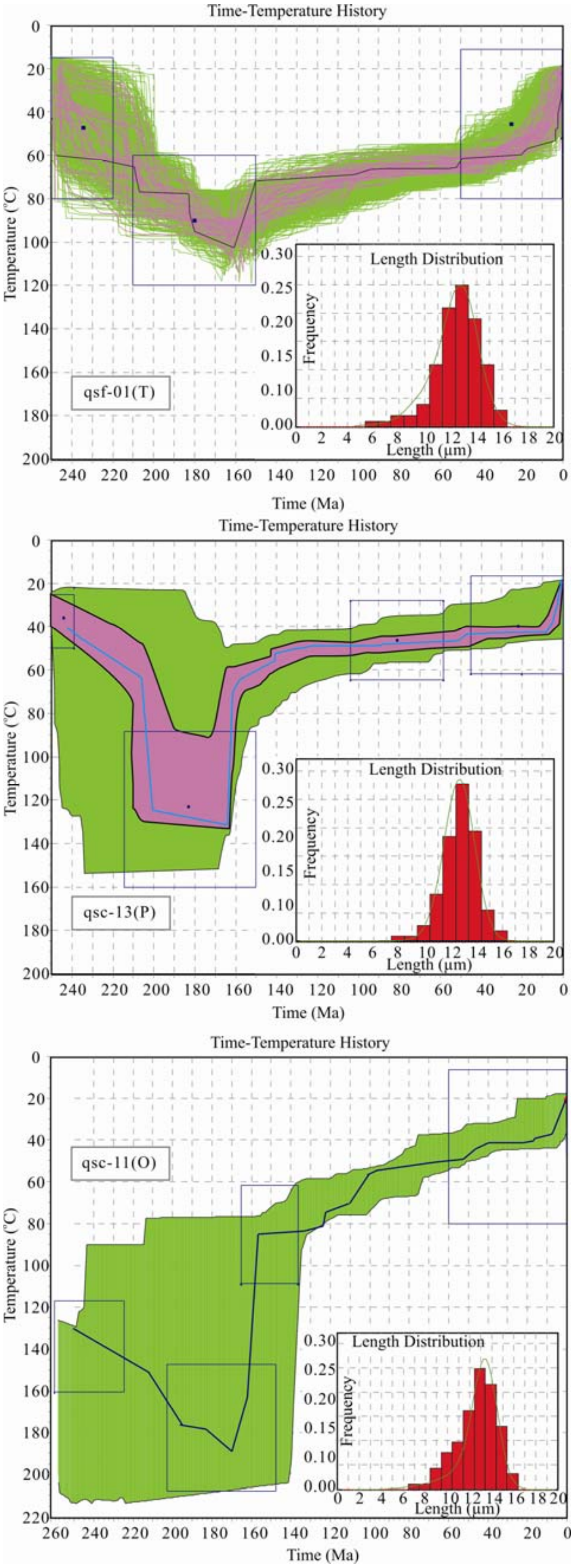

Fig. 4. Cooling history recovery by fission-track for three samples.

The sample of qsc-13, which belongs to the Upper Permian, experienced an increasing burial-temperature after its sedimentation, and the maximum paleotemperature in Late Jurassic (~163 Ma) with ~132°C. After that, the Permian experienced four stages of cooling evolutionary history: a rapidly cooling phase of (~163 Ma - ~140 Ma) with temperature decreasing from ~132°C to ~53°C and a cooling rate of ~3°C/Ma; a slow cooling phase of (~140 Ma to ~52 Ma) with temperature decreasing from ~53°C to ~47°C, a cooling rate less than ~0.1°C/Ma; a relatively slow cooling phase (~52 Ma to ~8 Ma) with the temperature from ~47°C to ~43°C and a cooling rate of ~0.1° C/Ma; and a rapid phase of temperature dropping from ~8 Ma to present, with temperature dropping to ~20°C and a cooling rate of ~3° C/Ma.

6.2 Uplift-erosion history reconstruction

Paleotemperature of formation was controlled by burial depth and paleogeothermal field. For stable regions without tectonic movement or magmatism, thermal gradient was considered to be constant and the cooling history of samples can be directly used to explain the history of strata uplift and denudation. While for some geological scenarios controlled by thermal anomalies, the temperature field must be discussed separately from burial subsidence and uplifting-denudation, so as to more accurately focus on the geological evolution process. Meanwhile, during the uplifting-erosion history reconstruction, not only the present geothermal gradient and the paleo-burial depth, but also the paleo-geothermal gradient and the corresponding erosion thickness should be taken into consideration during the reconstruction of the thermal evolution.

Paleo-temperature was reconstructed from the geothermal gradient and ancient burial thickness (Yu et al., 2018). From the analysis above, it can be seen that during the Triassic, some areas experienced a thermal anomaly and the geothermal gradient increased under the influence of intrusive rocks around the southwest Ordos Basin. After that, as the thermal anomaly decayed, the temperature gradient decreased correspondingly. Since late Jurassic, this region experienced several uplift-denudation processes. The paleogeothermal gradient since late Jurassic in this area would gradually decrease, not suddenly change.

The Chun2 well which is an exploratory well for natural gas in the southwest part of the Ordos Basin (Fig.1) includes the Cretaceous, the Jurassic, the Triassic, the Permian, the Carboniferous and the Ordovician from the top to the bottom. The total erosion thickness since the Late Cretaceous was about ~1000 m was calculated using the method of Vitrinite reflectance (Ren et al., 2014). Both the Qishan area and the Chun2 well are located in the southwest of the Ordos Basin and should have a similar sedimentary history. Based on the analysis method of sedimentary and denudation thickness trends (Ni et al., 2011), it is estimated that the total erosion thickness of the Qishan area since the Jurassic was about ~3350 m.

Assumptions for modeling were proposed in the process of paleo-thickness restoration, such as unchanging width of rocks in a horizontal direction, sediment framework with variable volume of pores during compaction in vertical direction, and compaction being considered an irreversible process. Based on the relationship equation of porosity-depth proposed by the previous studies (Yu, 2009), parameters such as porosity, buried depth, compression coefficient of the Ordos Basin made by previous work (Yu, 2009, 2012;Yu et al., 2017) were used to calculate the porosity with depth. The paleo-thickness of the strata at any time during the geological evolution could be calculated by the mathematical integral of porosity-depth calculation formula (Allen and Allen, 1990).

3D modeling is a powerful tool to recover the geological history (Yu, 2009; Yu, 2012; Li et al., 2013; Pang et al., 2017a, 2017b). Based on the assumptions above and simulation parameters by previous studies (Yu and Ren, 2008; Yu et al., 2012; Yu et al., 2017), the burial -thermal evolutionary history of the Kangjiazhuang area was established by using the *P*etromod software (Fig. 6) with the following data: the results of paleo-thickness and burial history restoration, the cooling rate and temperature decreasing value of samples, the time of maximum paleogeothermal occurrence, the paleogeothermal gradient discussed above and the thermal conductivity values for each set of strata. The present-day average ground-surface temperature of the Linyou - Qishan area is 11.9°C (Cao et al., 2016). Data of bitumen reflectance and thermal conductivity from samples of the qsf-01, the qsc-13, the qsu-01, and the qsu-02 were also used.

The tectonic uplift can be divided into several stages with corresponding erosion thickness. In the process, as the total erosion thickness of ~3350 m was the key parameter for the modeling, each thickness of the three stages maybe modified if the calculated temperature and the geochronological temperature didn't match well. Only

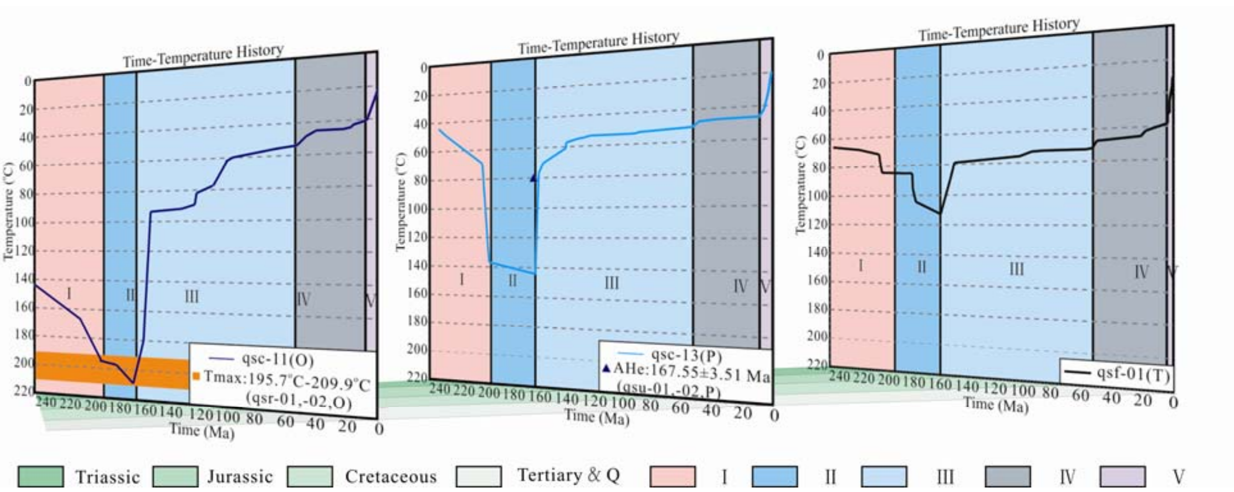

Fig. 5. Modeling results of three samples.
(I) Rapid heating: dual effect due to deposition and a thermal event; (II) slow heating: subsidence-burial process; (III) discrepant rapid cooling - slow cooling; (IV) slow cooling-uplift; (V) rapid cooling-uplift process.

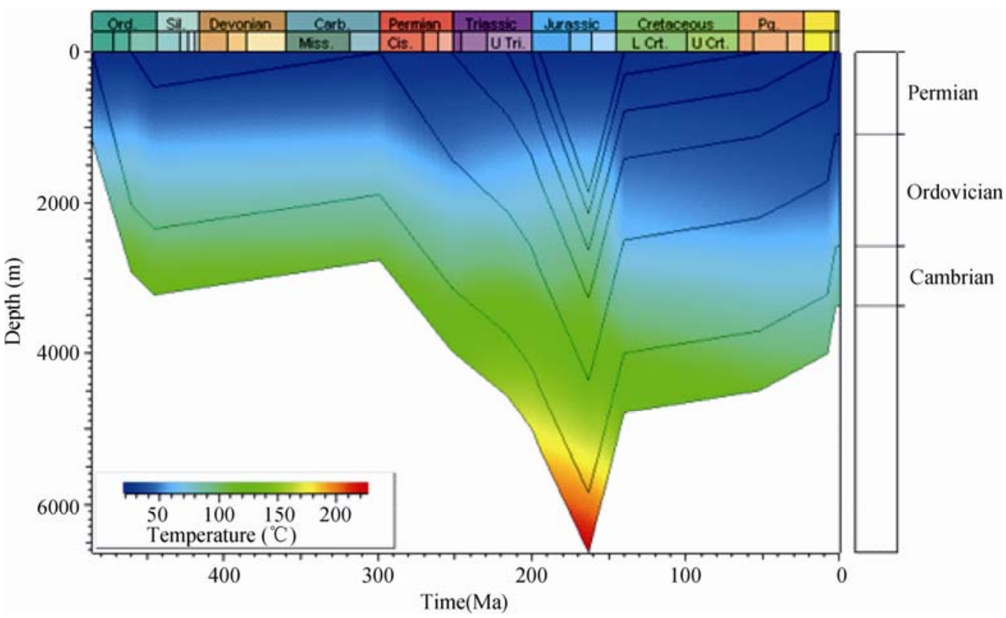

Fig. 6. Tectonic thermal evolution of the Kangjiazhuang area.

when the fitness is high enough, the erosion thickness of each stage can really reflect the period, rate and range of the process of uplifting (Ren et al., 2006; Yu, 2009; Yu et al., 2012).

The tectonothermal evolutionary history of the Qishan area was as follows (Fig. 6): a stage of sedimentation from early Permian to middle Jurassic with a peak deposition rate in Triassic. Maximum temperature existed at ~163 Ma. Uplifting- cooling since late Jurassic with four stages, ~163 Ma to ~140 Ma, ~140 Ma to ~52 Ma, ~52 Ma to ~8 Ma, ~8 Ma to present. The uplift amplitude of the Permian from ~163 Ma to ~140 Ma was about ~1900 m with an uplift rate of ~82 m/Ma. From ~140 Ma to ~52 Ma, the erosion thickness of ~300 m with an uplift rate of ~3 m/Ma. From ~52 Ma to ~8 Ma, the erosion thickness of ~500 m with an uplift rate of ~11 m/Ma. Since ~8 Ma, an erosion thickness of ~650 m and an uplift rate of ~81 m/Ma.

In conclusion, the tectonothermal evolutionary history of the Qishan area can be summarized as follows: During Triassic, subsidence and burial depth of strata in this region increased rapidly. Affected by the collision between the North China Plate and the Yangtze Plate and the movement of the Qinling Orogeny, these strata underwent a rapid increase of geothermal temperature. Since late Jurassic, all the strata uplifted. From early Cretaceous to early Eocene, different area in the southwest Weibei Uplift featured as differential cooling-uplift rate. In the area where the qsf-01 located, the cooling rate decreases gradually with continuous uplift; In the area where samples of the qsc-13 and the qsc-11 located, the strata uplift amplitude was small and the temperature change was not significant. From early Eocene at ~52 Ma to late Miocene at ~8 Ma, all the strata uplifted and cooled with a gradually increasing rate. Since late Miocene at ~8 Ma, the Qishan area has a similar uplift rate and cooling rate in the outcropping zones of each set of strata as a whole.

6.3 Implications for the tectonothermal evolutionary history

The tectonothermal evolutionary history obtained by modeling is consistent with the present tectonic features and stratigraphic contact relationship of the research area. The relationship of the Qishan area to its surroundings appears to be an evolutionary history coupling with the response of stratigraphic contact and strata thickness, such as the conformable contact between the Jurassic strata and the Cretaceous strata in the area far away from the north of the research area, an angular unconformity between the Jurassic strata and the Cretaceous strata in the Qishan area. Unlike the erosional evolutionary history of the Qishan area, the Weihe Basin which is located to the south of the Qishan area underwent a relatively unique evolutionary history as it was buried by a thick succession of sedimentary deposits since the period of the Himalayan movement.

From published thermochronology data of the Qishan–Linyou area of the Weibei Uplift (Ren et al., 1995; Qi et al., 2015; Wang et al., 2010; Xiao et al., 2013; Ren et al., 2014; Ren et al., 2015a), some geological scenarios had been concluded: (1) AFT data analysis showed that the maximum paleogeothermal gradient of the Ordos Basin were happened in late Mesozoic with highest strata temperature (Ren et al., 1995). (2) Early uplift in the east and in the west (114–106 Ma), late uplift in the middle and in the north (86 Ma) of the Weibei Uplift (Wang et al., 2010). (3) three stages of uplift, 146–125 Ma, 107–83.8 Ma and 40–27.3 Ma (Xiao et al., 2013). (4) Strata in the northern part of the Weibei Uplift, the Hancheng area, and the Hejin area all underwent rapid uplift at 40 Ma, especially after 5 Ma (Ren et al., 2015a). (5) The Eocene (40 Ma) and the Late Miocene (8 Ma) are critical times for the cooling of the oil shale (Yu et al., 2018).

The Linyou area is located northeast to the Qishan area. The sample Wq-75 of the Upper Triassic in the Linyou area (Wang et al., 2010) has a mixed age of 125±7 Ma with $P(\chi^2)$ =0.1%. And there were 111 fission tracks with an average value of 11.7±7 μm. Two peak ages of 114 Ma and 146 Ma were got after the Gaussian Fitting. The $P(\chi^2)$ of five samples from the Upper Ordovician to the Middle Triassic in the Waguanling area is less than 5.0% (Xiao et al., 2013), which indicated that all these samples had mixed source. The peak age obtained by Gaussian fitting is between 40–138 Ma. Apatite peak ages of the Ordovician and the Permian strata in the Caojiagou area (northeast of the Qishan county) were 75 Ma and 128–134 Ma (Qi et al., 2015). In all, there were mainly three periods of peaks of AFT age in the Linyou area: 146–125 Ma, 107–83.8 Ma, and 40–27.3 Ma, reflecting three main cooling processes: Early Cretaceous, Late Cretaceous and Eocene–Oligocene.

In contrast, located in the southwest margin of the Weibei Uplift, the south Qishan area underwent an earlier uplift-cooling history compared to other parts of the Weibei Uplift. In late Jurassic, the Qinling Orogenic Belt experienced a multicycle intracontinental orogenesis (Dong and Santosh, 2016) and the Qishan area was influenced by a north-south stress of the Paleo-Tethys Domain which resulted in the uplift - denudation movement. The study area underwent intense regional tectonic movements in late Cretaceous (Liu et al., 2006; Zhao et al., 2018). The continuous uplift of this region since late Jurassic can be divided into in four stages with distinct difference in uplift rate, erosion thickness, cooling rate and temperature changes. The most rapid cooling and uplift commenced at ~8 Ma.

7 Conclusions

Using methods of thermochronology and geothermometry, this paper reconstructed the uplift - cooling and denudation history of the Permian outcrop zone in the Qishan area, Ordos Basin since Mesozoic.

(1) The tectonothermal evolution history of the Qishan area since Mesozoic was controlled by the interaction of the Qinling Orogenic Belt and the Weibei Uplift. Under a rapid subsidence in Triassic, the Permian strata was heated rapidly. During late Jurassic, the burial continued, but the temperature gradient gradually decreased. From late Jurassic to late Eocene, the differential evolution of denudation, uplift and cooling occurred in different

outcrops. After that, the Qishan area began a rapid cooling -uplift phase during late Miocene to Present. Each evolutionary stage of the Permian strata was consistent with the present stratigraphic of this region, and coupling with the Qinling Orogenic Belt and the Weihe Basin.

(2) The south Qishan area experienced a maximum paleotemperature of ~132°C in late Jurassic at ~163 Ma. A stage of rapid cooling (~132°C to ~53°C) occurred between ~163 Ma to ~140 Ma at a rate of ~3°C/Ma; a stage of slow cooling (~53°C to ~47°C) between ~140 Ma to ~52 Ma at a rate less than 0.1°C/Ma; a stage of slow cooling (~47°C to ~43°C) between ~52 Ma to ~8 Ma at a rate of ~0.1°C/Ma; and a period of rapid cooling to ~20°C at a rate of ~3°C/Ma since ~8 Ma.

(3) An estimated thickness of ~1900 m sediment was removed in the Qishan area between ~163 Ma to ~140 Ma with a uplifting rate of ~82 m/Ma; an erosion thickness of ~300 m occurred during ~140 Ma to ~52 Ma with an uplift rate of ~3 m/Ma; an erosion thickness of ~500 m occurred during ~52 Ma to ~8 Ma with an uplift rate of ~11 m/Ma; an erosion thickness of ~650 m occurred during ~8 Ma to present with an uplift rate of ~81 m/Ma.

(4) The south Qishan area has an earlier uplift-cooling history compared to other parts of the Weibei Uplift. Early Eocene at ~52 Ma and late Miocene at ~8 Ma were two key time for the uplift-cooling history of the southwest Weibei Uplift.

Acknowledgements

We acknowledge comments and suggestions from Barry Kohn from the University of Melbourne and two anonymous reviewers, language polishing from Barry Kohn. Thanks should be given to the guidance of fission track experimental process by Ling Chung and zircon (U-Th)/ He dating by Abaz Alimanović, both from the University of Melbourne, as well as apatite (U-Th)/ He dating by Jingbo Sun from the Isotope Thermochronology of the Institute of Geology of the Chinese Academy of Geosciences. We also thank Daniel James Lehrmann from the Trinity University for language polishing. This work is granted by the Project "Constraints on lithospheric dynamic evolution and hydrocarbon accumulation from Late Mesozoic paleogeothermal field in Ordos and Qinshui Basins supported by NSFC (41630312)", the "Palaeogeothermal and uplift-related cooling history of complex structure zone, Restricted by thermochronology by NSFC (41602128)", the NSFC (41703055), the "research Grants by China Geological Survey (DD20160060)", the "Fundamental Research Funds for the Central Universities, CHD (300102279206, 300102278204)", and the fund from China Scholarship Council (201806565017).

Manuscript received Sept. 4, 2018
accepted Apr. 14, 2019
associate EIC YANG Jingsui
edited by FEI Hongcai

References

Allen, P.A., and Allen, J.R., 2005. Basin analysis: Principles and applications (2rd edition). Oxford: Blackwell Science.

Barker, C.E., and Pawlewica, M.J., 1986. The correlation of vitrinite reflectance with maximum temperature in humic organic matter. Lecture Notes in Earth Science, 5, 79–81.

Cao, Z.P., Ren, Z.L., Xiong, P., Qi, K., and Chen Z.J., 2016. The Ordovician thermal evolution and hydrocarbon generation history in the southwestern margin of Weibei uplifting of the Ordos Basin: a case study of the Linyou-xunyi region. Acta Geologica Sinica, 90(3): 513–520 (in Chinese with English abstract).

Chen, Y.Z., Fu, X.F., Xiao, A.C., Yu, L., Tang, Y., and Mao, L., 2015. Type and evolution of carbonate platforms in Jixian Period Mesoproterozoic: southwestern margin of Ordos Basin. Journal of Petroleum Exploration and Production Technology, 6(4): 555–568 (in Chinese with English abstract).

Chen, Z.X., Zeng, Z.G., Wang, X.Y., Yin, X.B., Chen, S., Guo, K., Lai, Z.Q., Zhang, Y.X., Ma, Y., Qi, H.Y., Wu, L., 2018. U-Th/He dating and chemical compositions of apatite in the dacite from the southwestern Okinawa Trough: Implications for petrogenesis. Journal of Asian Earth Sciences, 161:1-13.

Donelick, R.A., O'Sullivan, P.B., Ketcham, R.A., 2005. Apatite fission-track analysis. Reviews in Mineralogy and Geochemistry, 58(1): 49–94.

Dong, Y.P., and Santosh, M., 2016. Tectonic architecture and multiple orogeny of the Qinling orogenic belt, Central China. Gondwana Research, 29(1): 1–40.

Du, Q.X., Han, Z.Z., Shen, X.L., Han, C., Song, Z.G., Gao, L.H., Han, M., and Zhong, W.J., 2018. Geochronology and geochemistry of Permo-Triassic sandstones in eastern Jilin Province (NE China): implications for final closure of the paleo-Asian Ocean. Geoscience Frontiers, 10(2): 683–704. DOI: doi.org/10.1016/j.gsf.2018.03.014.

Fan, A.P., Yang, R.C., Loon, A.J., Yin, W., Han, Z.Z., and Zavala, C., 2018. Classification of gravity-flow deposits and their significance for unconventional petroleum exploration, with a case study from the Triassic Yanchang Formation (southern Ordos Basin, China). Journal of Asian Earth Sciences, 161: 57–73.

Farley, K.A., 2000. Helium diffusion from apatite: general behavior as illustrated by Durango fluorapatite. Journal of Geophysical Research: Solid Earth, 105(B2): 2903–2914.

Farley, K., Wolf, R., and Silver, L., 1996. The effects of long alpha-stopping distances on (U–Th)/He ages. Geochim Cosmochim Ac, 60 (21):4223–4229.

Feng, G.X., and Chen, S.J., 1988. Relationship between the reflectance of bitumen and vitrinite in rock. Natural Gas Industry, 8(3): 7, 20–25 (in Chinese with English abstract).

Gleadow, A.J.W., Belton, D.X., Kohn, B.P, and Brown, R.W., 2002. Fission track dating of phosphate minerals and the thermochronology of apatite. Reviews in Mineralogy and Geochemistry, 48(1): 579–630.

Gleadow, A. J.W., Harrison, M., Kohn, B., Zazueta, R.L., and Phillips, D., 2015. The Fish Canyon tuff: A new look at an old low-temperature thermochronology standard. Earth and Planetary Science Letters, 424: 95–108.

Gong, W.B., Hu, J.M., Wu, S.J., Chen, H., Qu, H.J., Li, Z.H., Liu, Y., and Wang, LJ., 2014. Possible southwestward extrusion of the Ordos Block in the Late Paleoproterozoic: constraints from kinematic and geochronologic analysis of peripheral ductile shear zones. Precambrian Research, 255: 716–733.

House, M., Kohn, B., Farley, K., Raza, A., 2002. Evaluating thermal history models for the Otway Basin, southeastern Australia, using (U–Th)/He and fission-track data from borehole apatites. Tectonophysics 349(1):277–295.

Hu, S.B., He, L.J., Zhu, C.Q., and Wang, J.Y., 2008. Method system of thermal reconstruction for marine basins. Oil & Gas Geology, 29(5): 607–613 (in Chinese with English abstract).

Huang, Z.G., Ren, Z.L., and Gao, L.G., 2016. Evidence from detrital zircon and apatite fission track for tectonic evolution since Cretaceous in southeastern margin of Ordos Basin. Chinese Journal of Geophysics (Acta Geophysica Sinica), 59 (10): 3753–3764 (in Chinese with English abstract).

Ketcham, R.A., 2005. Forward and inverse modeling of low-temperature thermochronometry data. Reviews in Mineralogy and Geochemistry, 58(1): 275–314.

Kohn, B.P., Chung, L., and Gleadow, A.J.W., 2019. Fission-track analysis: Sample preparation and data collection. Chapter 2. In: Malusà, M.G., and Fitzgerald, P.G. (eds.), Fission track thermochronology and its application to geology. Switzerland: Springer-Verlag.

Laslett, G., Green, P.F., Duddy, I., Gleadow, A., 1987. Thermal annealing of fission tracks in apatite 2. A quantitative analysis. Chem Geol: Isot Geosci Sect 65(1):1–13.

Li, G.W., Kohn, B., Sandiford, M., Xu, Z.Q., and Wei, L.J., 2015. Constraining the age of Liuqu conglomerate, Southern Tibet: Implications for evolution of the India-Asia collision zone. Earth and Planetary Science Letters, 426: 259–266.

Li, X., Zhang, J.L., Yuan, Y., Li, C.L., and Meng, N.N., 2013. Sequence stratigraphic analysis and integrated 3D geological modeling of M1 block, Wenmingzhai oilfield, Dongpu depression, China. Central European Journal of Geosciences, 5(3): 374–386.

Li, Y., Chang, X.C., Yin, W., Sun, T.T., and Song, T.T., 2017. Quantitative impact of diagenesis on reservoir quality of the Triassic Chang 6 tight oil sandstones, Zhenjing area, Ordos Basin, China. Marine and Petroleum Geology, 86: 1014–1028.

Liu, C.Y., Zhao, H.G., Wang, F., and Chen, H., 2005. Attributes of the Mesozoic structure on the west margin of the Ordos Basin. Acta Geologica Sinica, 79(6): 737–747 (in Chinese with English abstract).

Liu, C.Y., Zhao, H.G., Gui, X.J., Yue, L.P., Zhao, J.F., and Wang, J.Q., 2006. Space-time coordinate of the evolution and reformation and mineralization response in Ordos Basin. Acta Geologica Sinica, 80(5): 617–638 (in Chinese with English abstract).

Malusà, M.G., and Fitzgerald, P.G., 2018. Fission-track thermochronology and its application to geology. Switzerland: Springer: 49–50.

McDowell, F.W., McIntosh, W.C., and Farley, K.A., 2005. A precise ^{40}Ar–^{39}Ar reference age for the Durango apatite (U-Th)/He and fission-track dating standard. Chemical Geology, 214(3–4): 249–263.

Ni, J.L., Guo, Y., Wang, Z.M., Liu, J.L., Lin, Y.X., and Li, Y., 2011. Tectonics and mechanisms of uplift in the central uplift belt of the Huimin depression. China University of Geosciences, 22(3): 299–315 (in Chinese with English abstract).

Ni, J.L., Liu, J.L., Tang, X.L., Yang, H.B., Xia, Z.M., and Zhang, T.T., 2016. Early Cretaceous exhumation of the Sulu orogenic belt as a consequence of the eastern Eurasian tectonic extension insights. Journal of the Geological Society, 173(3): 531–549.

Pang, Y.M., Guo, X.W., Han, Z.Z., Zhang, X.H., Zhu, X.Q., Hou, F.H., Han, C., Song, Z.G., and Xiao, G.L., 2019. Mesozoic-Cenozoic denudation and thermal history in the central uplift of the South Yellow Sea Basin and the implications for hydrocarbon systems: constraints from the Csdp-2 borehole. Marine and Petroleum Geology, 99: 355–369.

Pang, Y.M., Zhang, X.H., Guo, X.W., Xiao, G.L., and Han, Z.Z., 2017a. Basin modeling in the initial stage of exploration: a case study from the North Subbasin of the South Yellow Sea Basin. Acta Oceanologica Sinica, 36(9): 65-78.

Pang, Y.M., Zhang, X.H., Guo, X.W., Xiao, G.L., and Zhu, X.Q., 2017b. Mesozoic and Cenozoic tectono-thermal evolution modeling in the Northern South Yellow Sea Basin. Chinese Journal of Geophysics, 60(8): 3177-3190, doi: 10.6038/cjg20170824 (in Chinese with English abstract).

Qi, K., Ren, Z.L., Cui, J.P., Yu, Q., Cao, Z.P., Yang, P., Deng, Y.R., and Zhang, M.T., 2015. The Meso-Cenozoic tectonic thermal evolution of the Qishan-linyou areas in Weibei uplift of Ordos Basin and its response in geology: evidence from fission-track analysis. Acta Geologica Sinica, 91(1): 151–162 (in Chinese with English abstract).

Qiu, N.S., Wang, J.Y., Mei, Q.H., Jiang, G., and Tao, C., 2010. Constraints of (U-Th)/He ages on Early Paleozoic tectonothermal evolution of the Tarim Basin, China. Science China Earth Sciences, 53(7): 964–976.

Qiu, X.W., Liu, C.Y., Mao, G.Z., Deng, Y., Wang, F.F., Wang, J.Q., 2013. Late Triassic tuff intervals in the Ordos Basin, Central China: their depositional, petrographic, geochemical characteristics and regional implications. Journal of Asian Earth Sciences, 80: 148–160.

Qiu, X.W., Liu, C.W., Mao, G.Z., Deng, Y., Wang, F.F., and Wang, J.Q., 2015a. Major, trace and platinum-group element geochemistry of the Upper Triassic nonmarine hot shales in the Ordos Basin, central China. Applied Geochemistry, 53: 42–52.

Qiu, X.W., Liu, C.Y., Wang, F.F., Deng, Y., and Mao, G.Z., 2015b. Trace and rare earth element geochemistry of the Upper Triassic mudstones in the southern Ordos Basin, Central China. Geological Journal. 50, 399-413.

Reiners, P.W., Farley, K.A., and Hickes, H.J., 2002. He diffusion and (U-Th)/He thermochronometry of zircon: initial results from Fish Canyon Tuff and Gold Butte. Tectonophysics 349:297–308.

Ren, Z.L., 1995. Application of apatite fission-track analysis method to the study of thermal history of the Ordos Basin. Chinese Journal of Geophysics, 38(2):233-247.

Ren, Z.L., Zhao, Z.Y., Zhang, J., and Yu, Z.P., 1994. Research on paleotemperature in the Ordos Basin. Acta Sedimentologica Sinica, 12(1): 56–65 (in Chinese with English abstract).

Ren, Z.L., Zhang, S., Gao, S.L., Cui, J.P., and Liu, X.S., 2006. Research on region of maturation anomaly and formation time in Ordos Basin. Acta Geologica Sinica, 80(5): 674–684 (in Chinese with English abstract).

Ren, Z.L., Cui, J.P., Li, J.B., and Wang, J.P., 2014. Tectonic - thermal history reconstruction of Ordovician in the Weibei uplift of Ordos Basin. Acta Geologica Sinica, 88(11): 2044–2056 (in Chinese with English abstract).

Ren, Z.L., Cui, J.P., Guo, K., and Tian, T., 2015a. Thermal history of Ordos Basin assessed by apatite fission track analysis. Science Bulletin, 60(14): 1298–1309.

Ren, Z.L, Cui, J.P., Liu, C.Y., Li, T.J., Chen, G., Dou, S., Tian, T., and Luo, Y.T., 2015b. Apatite fission track evidence of uplift cooling in the Qiangtang Basin and constraints on the Tibetan Plateau Uplift. Acta Geological Sinica (English Edition), 89(2): 467–484. https://doi.org/10.1111/1755-6724.12441.

Shi, B.B., Chang, X.C., Yin, W., Li, Y., and Mao, L.X., 2019. Quantitative evaluation model for tight sandstone reservoirs based on statistical methods - a case study of the Triassic Chang 8 tight sandstones, Zhenjing area, Ordos Basin, China. Journal of Petroleum Science and Engineering, 173: 601–616 (in Chinese with English abstract).

Song, Y., Stepashko, A., Liu, K.Y., He, Q.K., Shen, C.B., Shi, B.J., and Ren, J.Y., 2018. Post-rift tectonic history of the Songliao Basin, NE China cooling events and post-rift unconformities driven by orogenic pulses from plate boundaries. Journal of Geophysical Research. Solid Earth, 123 (3): 2363–2395.

Song, Z.G., Han, Z.Z., Gao, L.H., Geng, H.Y., Li, X.P., Meng, F., Han, M., Zhong, W., Li, J., Du, Q., Yan, J., and Liu, H., 2018. Permo-Triassic evolution of the southern margin of the Central Asian orogenic belt revisited: insights from Late Permian igneous suite in the Daheishan horst, Ne China. Gondwana Research, 56: 23-50.

Suggate, R.P., 1998. Relations between depth of burial, vitrinite reflectance and geothermal gradient. Journal of Petroleum Geology, 22(2): 5–32.

Tao, N., Li, Z.X., Danisik, M., Evans, N.J., Batt, G.E., Li, W.X., Pang, C.J., Jourdan, F., Xu, Y.G., and Liu, L.P., 2017. Thermochronological record of middle–late Jurassic magmatic reheating to Eocene rift-related rapid cooling in the SE South China Block. Gondwana Research, 46: 191–203.

Vermeesch, P., 2009. RadialPlotter: a Java application for fission track, luminescence and other radial plots. Radiation Measurements, 44, 4, 409-410.

Wang, C., Liu, L., Korhonen, F., Yang, W.Q., Cao, Y.T., He, S.P., Zhu, X.H., Liang, W.T., 2016. Origins of Early Mesozoic granitoids and their enclaves from West Kunlun, NW China implications for evolving magmatism related to closure of the Paleo-Tethys Ocean. Springer Berlin Heidelberg, 105(3): 941–964.

Wang, G.W., Chang, X.C., Yin, W., Li, Y., and Song, T.T., 2017. Impact of diagenesis on reservoir quality and heterogeneity of the Upper Triassic Chang 8 tight oil sandstones in the Zhenjing area, Ordos Basin, China. Marine and Petroleum Geology, 83: 84-96.
Wang, J.Q., Liu, C.Y., Yan, J.P., Zhao, H.G., Gao, F., and Liu, C., 2010. Development time and evolution characteristics of Weibei uplift in the south of Ordos Basin. Journal of Lanzhou University (Natural Sciences), 46(4): 22–29 (in Chinese with English abstract).
Wang, X.S., Zhang, X., Gao, J., Li, J.L., Jiang, T., and Xue, S.C., 2018. A slab break-off model for the submarine volcanic-hosted iron mineralization in the Chinese Western Tianshan: Insights from Paleozoic subduction-related to post-collisional magmatism. Geology Reviews, 92: 144–160 (in Chinese with English abstract).
Xiao, H., Li, J.X., Han, W., and Yang, Q.J., 2013. The tectonic uplift time and evolution characteristics of Weibei uplift in the south edge of Ordos Basin. Journal of Xi'an University of Science and Technology, 33(5): 576–593 (in Chinese with English abstract).
Yang, R.C., He, Z.L., Qiu, G.Q., Jin, Z.J., Sun, D.S., and Jin, X.H., 2014. A late Triassic gravity flow depositional system in the southern Ordos Basin. Petroleum Exploration and Development, 41(6): 724–733 (in Chinese with English abstract).
Yang, R.C., Jin, Z.J., Loon, A.J., Han, Z.Z., and Fan, A.P., 2017. Climatic and tectonic controls of lacustrine hyperpycnite origination in the late Triassic Ordos Basin, central China. AAPG Bulletin, 101(1): 95–117.
Yu, Q., and Ren, Z.L., 2008. Comparison of geothermal fields in the Huangling and Dongsheng areas, Ordos Basin. Journal of Jilin University (Earth Science Edition), 38(6): 933–936, 945 (in Chinese with English abstract).
Yu, Q., 2009. The thermal evolution history of Ordos Basin Mesozoic and relationship with various energy mineral deposit (MA. thesis). Xi'an: Northwest University (in Chinese with English abstract).
Yu, Q., Ren, Z.L., Wang, B.J., Gao, L.J., Li, C.F., and Cao, H.X., 2012. Thermal evolution history of the upper Paleozoic in Yanchang exploratory area, Ordos Basin. Geological Review, 58(2): 303–308 (in Chinese with English abstract).
Yu, Q., 2012. The Paleozoic thermal evolution history and natural gas accumulation of the central and eastern Parts of Ordos Basin (Ph.D. thesis). Xi'an: Northwest University (in Chinese with English abstract).
Yu, Q., Ren, Z.L., Li, R.X., Wang, B.J., Qin, X.L., and Tao, N., 2017. Paleogeotemperature and maturity evolutionary history of the source rocks in the Ordos Basin. Geological Journal, 52 (S1): 97–118.
Yu, Q., Ren, Z.L., Zhu, Z.W., Tao, N., Wang, B.J., and Li, C.C., 2018. Exhumation, cooling and erosion history of Triassic oil shale since Late Cretaceous, Binxian-Tongchuan area of Ordos Basin. Earth Science, 43(6): 1839–1849 (in Chinese with English abstract).
Zhang, X., Feng, Q., Sun, P., Li, W., 2010. Characteristics of high gamma ray reservoir of Yanchang formation in Ordos basin. Chinese Journal of Geophysics Chinese Edition, 53, 205-213 (in Chinese with English abstract).
Zhao, G.C., Wilde, S.A., Guo, J.H., Cawood, P.A., Sun, M., and Li, X.P., 2010. Single zircon grains record two Paleoproterozoic collisional events in the North China Craton. Precambrian Research, 177(3): 266–276.
Zhao, X.C., Liu, C.Y., Wang, J.Q., and Zhao, Y., 2018. Mesozoic geological events and its evolution sequence of the northern North-South tectonic belt, China. Geological Review, 64(6):1324-1338 (in Chinese with English abstract).
Zuo, Y.H., Ye, B., Wu, W.T., Zhang, Y.X., Ma, W.X., Tang, S.L., and Zhou, Y.S., 2017. Present temperature field and Cenozoic thermal history in the Dongpu depression, Bohai Bay Basin, North China. Marine and Petroleum Geology, 88: 696–711.

About the first author

YU Qiang, male, born in 1983 in Shaanxi Province, is currently an associate professor at the School of Earth Science and Resources, Chang'an University. His research interests focus on tectonothermal history recovery using thermochronology and geothermometry for petroleum accumulation and structural ore-forming model. E-mail: yuqiang@chd.edu.cn.

About the corresponding author

REN Zhanli, male,born in 1961 in Shaanxi Province, is currently a professor at the Department of Geology, Northwest University. His academic interests focus on research of tectonic thermal history recovery for sedimentary basins and Orogeny as well as petroleum accumulation, exploration, and geothermal resources. E-mail: renzhanl@nwu.edu.cn.